



## Charge redistribution in FeOOH nanoarray by ecological oxygen-reduction deposition for boosting electrocatalytic water oxidation

Yaotian Yan <sup>a,1</sup>, Keke Huang <sup>a,1</sup>, Jinghuang Lin <sup>b,1</sup>, Taili Yang <sup>a</sup>, Peijia Wang <sup>a</sup>, Liang Qiao <sup>c</sup>, Wei Cai <sup>a</sup>, Xiaohang Zheng <sup>a,\*</sup>

<sup>a</sup> School of Materials Science and Engineering, Harbin Institute of Technology, Harbin 150001, China

<sup>b</sup> Institute of Engineering Innovation, The University of Tokyo, Tokyo, Japan

<sup>c</sup> Key Laboratory of Materials Design and Quantum Simulation, College of Science, Changchun University, Changchun 130022, China



### ARTICLE INFO

**Keywords:**

Deposition  
Oxygen reduction  
Oxygen evolution reaction  
Charge redistribution  
Electrocatalysis

### ABSTRACT

The exploration for economic and ecological strategies to fulfill macro-synthesis of highly efficient nanoelectrocatalysts has always been a key concern for electrocatalytic energy conversion field. Herein, a room-temperature oxygen-reduction deposition method was proposed to achieve the scaled-up preparation of Ni incorporated polycrystalline FeOOH (Ni-FeOOH) nanosheets on Fe metal. Due to the reduction potential difference between Fe metal and O<sub>2</sub> in the atmosphere, the O<sub>2</sub> reduction would thermodynamically occur in the designed Ni<sup>2+</sup> liquid layer covered on Fe metal. Therefore, Ni-FeOOH nanosheets would be in-situ generated on the surface within a short cycle of 20 min. Furthermore, the Ni heteroatom induced the charge redistribution in FeOOH, where the average valence of both Fe and Ni cations was shifted to high states. As a result, the decreased Fermi level and increased electron acceptor significantly reduced the energy barrier of rate-determining step (by ~1.4 eV). Finally, polycrystalline Ni-FeOOH shows a low overpotential of 239 mV at 10 mA/cm<sup>2</sup>, a low Tafel slope of 33 mV dec<sup>-1</sup>, and a dramatically increased TOF value (32.6 times higher than pristine sample), which even surpass some mainstream electrocatalysts consisting of noble-metal composition. This work provides an in-depth insight on Ni-Fe interaction mechanism, as well as a highly economic and ecological strategy to design and synthesize scaled-up FeOOH based electrocatalysts for water oxidation.

### 1. Introduction

The oxygen evolution reaction (OER) plays a significant role in renewable electrocatalytic fields such as water decomposition, CO<sub>2</sub> reduction and metal-air battery. However, the sluggish four-electron transfer process in OER greatly limited the overall efficiency of application device [1,2]. To facilitate OER process, high performance electrocatalysts were urged to reduce the energy barrier of rate-determining step. The mainstream noble metal-based electrocatalysts (such as IrO<sub>2</sub> and RuO<sub>2</sub>) exhibit excellent intrinsic activity for OER, but scarcity and high cost hinder their scaled-up manufacturing and commercial applications [3,4]. Therefore, exploration and synthesis towards non-noble metal electrocatalytic materials with high OER activity has become a key concern for related energy conversion technologies.

Recently, 3d-transition-metal oxides, hydroxides and hydroxyl oxides have been benchmarked as potential OER electrocatalysts in

alkaline media [5–10]. Among them, Fe based compounds are recognized as the most cost-effective candidates, because of the rich Fe crustal abundance (5.6%) and low materials cost [11,12]. Previous reports have applied FeOOH for OER electrocatalysis, and pointed out that most Fe based electrocatalysts (nitride, sulfide, phosphide, selenide, carbide etc.) would transform into FeOOH during OER to work [13,14]. However, the conductivity of FeOOH is insufficient, and the adsorption energy for OER intermediates is far from ideal states [15–18].

To address above issue, a research frontier is intending to design high-valent transition metal states to enhance intrinsic OER activities (such as charge and mass transferring properties) [19]. Generally, transition metal element (typically Fe<sup>3+</sup> in most catalysts) would be transformed to Fe<sup>4+</sup> first during OER and then Fe<sup>4+</sup> would contribute as actual active sites [20]. The high valence correlates with rich holes in valence band of catalyst, which benefits for serving as electrons acceptor and transferring negatively charged OER intermediates (such as OH<sup>-</sup>,

\* Corresponding author.

E-mail address: [zhengxiaohang@hit.edu.cn](mailto:zhengxiaohang@hit.edu.cn) (X. Zheng).

<sup>1</sup> These authors contribute equally.

$O^{2-}$ ,  $OOH^-$ ). Therefore, if high-valent  $Fe^{4+}$  sites are stabilized at ground state of electrocatalyst, the overpotential is expected to be reduced, due to the saved voltage and optimized adsorption energy. However, the Fe valence in most cases such as Ni-Fe LDH [21], Co-Fe LDH [22], Zn-Fe LDH [23], FeCoNiMnCu high entropy alloy etc. [24] derived by common liquid phase synthesis and high-temperature annealing is still limited to +3 at most. New strategy is still urged to be explored for designing high-valent catalyst. Besides, from a synthetic perspective, the commonly applied methods (such as hydrothermal and chemical vapor deposition methods) require huge heat energy consuming and long reaction time, which hinders large-scale preparation and commercial application. The synthesis strategy with low-cost effectiveness and feasible operation for scaled-up green preparation of nano-electrocatalysts is in urgent need.

Herein, inspired by the reduction potential difference between Fe metal ( $Fe^{2+} + 2e^- \rightarrow Fe$ ,  $\psi = -0.44$  V), Ni cation ( $Ni^{3+} + e^- \rightarrow Ni^{2+}$ ,  $\psi = 0.49$  V) and  $O_2$  ( $O_2 + 4 H^+ + 4e^- \rightarrow 2 H_2O$ ,  $\psi = 1.23$  V), we notice that the  $Ni^{2+}/Ni^{3+}$  transform is allowed to occur under the driven of oxygen, which is favorable for upshifting Fe valence and stabilizing high-valent state. A highly economical oxygen-reduction deposition strategy is proposed for in-situ synthesizing Ni incorporated FeOOH nanosheets with high-valent Fe site in room-temperature atmosphere. Low dose Ni heteroatoms (~7 a.t.%) on FeOOH surface own the capacity for shifting the average valence to high states, which decreases Fermi level and increases electron acceptor. As a result, energy barrier of rate-determining step is reduced by ~1.4 eV, which accounts for outstanding OER activity in alkaline media with small Tafel slope of 33 mV/dec and an overpotential of 239 mV at 10 mA/cm<sup>2</sup>. Current method affords unique advantages of short synthetic period (~20 min) and ultralow synthetic costs (no requirement for high temperature/pressure and noble ingredients), which owns potential as fast platform for exploring low cost and high-efficiency FeOOH based nano-electrocatalysts.

## 2. Experiment section

### 2.1. Setup of oxygen-reduction deposition (ORD) method

The oxygen-reduction deposition process originates from the reduction potential difference between Fe substrate and  $O_2$  in the thin liquid layer. By a facile room-temperature immersion in  $NiCl_2$  solution, the thin liquid layer containing Ni cation would be covered on Fe network surface. While placing in the air, the  $O_2$  would diffuse into liquid layer. The REDOX potential difference between Fe network and  $O_2$  would drive the oxygen-reduction deposition process to generate nanosheets on Fe surface.

### 2.2. Synthesis of Ni-FeOOH nanosheets

Fe network was sequentially washed by dilute HCl, ethanol and deionized water several times with ultrasonic to remove surface oxide layer for further use. Then the Fe network was immersed in  $NiCl_2$  solution to completely wet the surface. After that, the Fe network covered with liquid layer was taken out and subjected to air. The ecological oxygen-reduction deposition process then spontaneously took place. After 20 min, the sample was washed with deionized water, and then was dried by a blower. The Ni decorated FeOOH nanosheets (Ni-FeOOH) sample was obtained.

To conduct process optimization, the  $NiCl_2$  solution with different concentrations (0.04 M, 0.12 M, 0.16 M and 0.2 M) was utilized to generate Ni decorated FeOOH nanosheets (Ni-FeOOH) with different Ni contents. Besides, the influence of different oxygen reduction deposition time (0 min, 5 min, 10 min, 20 min and 40 min) was also explored. Through preliminary experiments, the sample derived by 0.16 M  $NiCl_2$  solution with oxygen reduction time of 20 min owned the optimal morphology and performance, which was marked as Ni-FeOOH. The

loading of Ni-FeOOH nanosheets on electrode was measured as ~2 mg cm<sup>-2</sup>.

### 2.3. Synthesis of FeOOH nanosheets

The FeOOH nanosheets were synthesized in the similar way as Ni-FeOOH nanosheets, except that the used solution was NaCl solution of 0.32 M. In current work, the source of  $Ni^{2+}$  comes from  $NiCl_2$ . To control variables in the synthesis process, the NaCl was used to provide  $Cl^-$ . The  $Cl^-$  is easily to adsorb on the Fe substrate surface and form soluble ferric chloride, which benefits for the release of Fe ions to liquid layer. Therefore, the subsequent oxygen reduction deposition reaction can occur smoothly.

### 2.4. Synthesis of Fe-soak sample

Fe-soak sample was prepared for contrast. Fe network was washed by dilute HCl, ethanol and deionized water several times with ultrasonic to remove surface oxide layer. After that, Fe network was immersed in  $NiCl_2$  solution with ultrasonic for 20 min, and then taken out for washing and drying by a blower. The Fe-soak sample was set for analyzing the influence of immersion with  $NiCl_2$  solution.

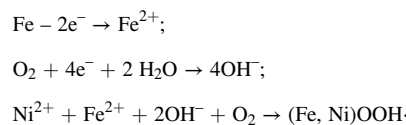
### 2.5. Synthesis of $IrO_2$ contrast sample

$IrO_2$  contrast sample was prepared by dispersing 50 mg of catalyst into 990  $\mu$ L of water/ethanol (v/v = 1:1) mixture and 10  $\mu$ L of 5 w.t.% Nafion through sonication for 60 min. Then 40  $\mu$ L  $IrO_2$  ink was dispersed onto Fe foam of 1 cm in geometric area to ensure a loading of ~2 mg cm<sup>-2</sup>.

## 3. Results and discussion

### 3.1. The synthetic process of Ni-FeOOH nanosheets

The Ni cation decorated FeOOH (Ni-FeOOH) nanosheets are synthesized through self-developed oxygen-reduction deposition method, which is performed at room temperature with a short cycle of 20 min (Fig. 1). After immersing Fe network in  $NiCl_2$  solution, a thin liquid layer with Ni cations would be covered on the Fe surface (Fig. S1). The oxygen in the air would diffuse spontaneously into the thin liquid layer, and then quickly contact with Fe. Due to the huge REDOX potential difference between  $O_2$  ( $O_2 + 2 H_2O + 4e^- \rightarrow 4OH^-$ ,  $\psi = 0.4$  V) and Fe substrate ( $Fe^{2+} + 2e^- \rightarrow Fe$ ,  $\psi = -0.44$  V), the Fe metal would be oxidized to  $Fe^{2+}$  cations spontaneously and then the Fe cations would dissolve in the liquid layer. At the same time, the  $Cl^-$  anion would adsorb on surface of fresh Fe metal and thus prevent the formation of oxidized passivation layer ( $FeO$ ,  $Fe_2O_3$  or other complex oxides), which benefits the continuous release of  $Fe^{2+}$  cation from Fe network and the formation of goal FeOOH product. Correspondingly, the dissolved oxygen in liquid layer would undergo a series of reduction process. Together with  $Ni^{2+}$  and  $Fe^{2+}$  in the liquid layer, the oxygen-reduction deposition process for Ni-FeOOH nanosheets is achieved as follows:



It should be noted that the REDOX potential of  $O_2/H_2O$  ( $\psi = 1.23$  V) is higher than those of  $Fe^{2+}/Fe^{3+}$  ( $\psi = 0.77$  V) and  $Ni^{2+}/Ni^{3+}$  ( $\psi = 0.49$  V), which determines that the transition from Fe,  $Ni^{2+}$  to  $Fe^{3+}$ ,  $Ni^{3+}$  is thermodynamics spontaneously driven by oxygen-reduction process. The  $\psi_{Fe^{2+}/Fe^{3+}}$  is higher than  $\psi_{Ni^{2+}/Ni^{3+}}$ , indicating that the  $Fe^{3+}$  is more favorable for binding anions. Thus, the main composition of final product is FeOOH based species.

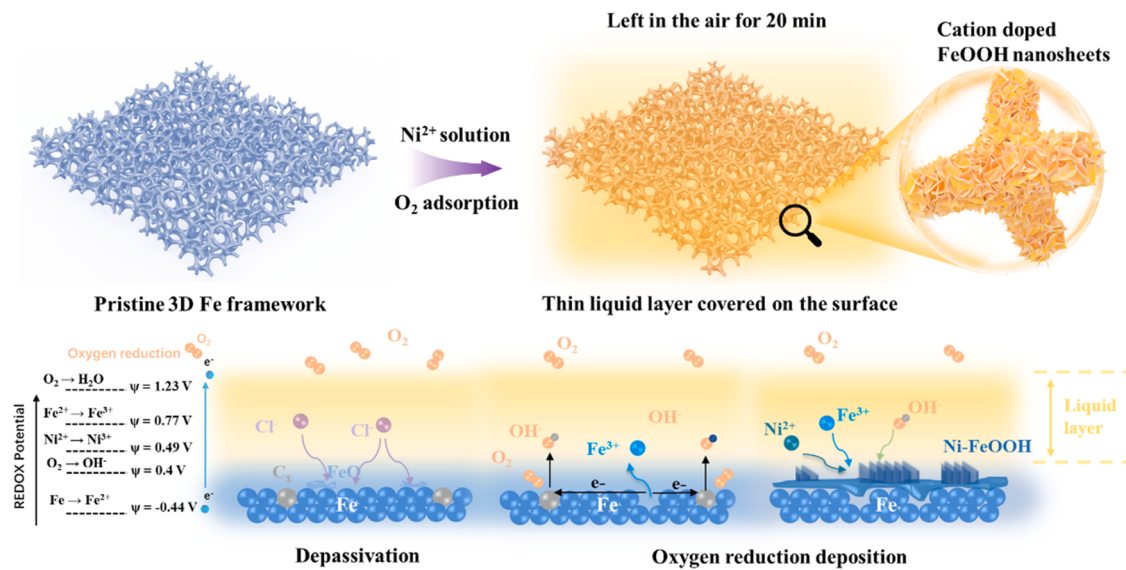


Fig. 1. The illustration of Ni-FeOOH nanosheets synthesis and oxygen-reduction deposition method.

### 3.2. The microstructure and strain states of FeOOH based electrodes

The microstructure of samples is characterized through scanning electron microscope (SEM) and transmission electron microscope (TEM) in Fig. 2. Pristine Fe network and Fe-Soak sample own the similar smooth surface (Figs. 2a and 2b), while after the oxygen-reduction deposition process, the vertically aligned nanosheets with an edge size of  $\sim 200$  nm are in-situ generated on the surface of Fe network (Fig. 2c). The influence of oxygen-reduction deposition time is further characterized in Fig. S2, where the nanosheets morphology is not found when the deposition time is less than 10 min. This excludes the possibility that the direct reaction of  $\text{NiCl}_2$  solution with Fe substrate leads to nanosheets formation. When the deposition time is longer than 10 min, the nanosheets morphology emerges, indicating that the oxygen diffuse and reduction reaction need a certain time to fulfill. The corresponding electrochemical tests are shown in Fig. S3, which suggests that the optimal deposition time is 20 min (with lowest overpotential (239.3 mV at  $10 \text{ mA/cm}^2$ ) and smallest Tafel slope (31.5 mV/dec) among samples derived by different deposition time). The influence of  $\text{NiCl}_2$  concentration is characterized in Fig. S4, where the optimal nanosheets morphology emerges under 0.16 M  $\text{NiCl}_2$  liquid layer. Furthermore, the corresponding electrochemical tests in Fig. S5 suggest that the optimal concentration is 0.16 M. It should be noted that the above-mentioned synthetic mechanism is based on the key role of oxygen reduction. The morphology of sample prepared without oxygen atmosphere is shown in Fig. S6, where no nanosheets are generated. This further confirms that the oxygen participation is indispensable condition for FeOOH nanosheets generation. The HADDF-STEM and element mapping in Fig. 2d further confirm the vertical nanosheets morphology and the uniform distribution of Ni, Fe, and O on Ni-FeOOH nanosheets. The well-defined lattice fringes with a d-spacing of  $\sim 0.21$  nm and  $\sim 0.13$  nm are displayed in the high-resolution TEM (HRTEM) image of Ni-FeOOH (Fig. 2e), which corresponds well to the (220) and (321) planes of FeOOH (JCPDS card no. 99-0055). The diffraction ring in selected area electron diffraction (SAED) image (Fig. 2e) further suggests that Ni-FeOOH nanosheets derived by as-proposed oxygen-reduction deposition method own a polycrystalline nature. Abundant grain boundary and lattice dislocation would inevitably exist in polycrystal, which is further confirmed by geometric phase analysis (GPA) along  $xx$  direction (Fig. 2f). According to definition, the lattice distortion is generated by crystal plane dislocation, atom displacement or vacancies, with a dramatic change in atomic coordination number. Around the distortions,

the atomic spacing will change sharply. Therefore, the lattice distortion would inevitably cause the surrounding lattice strain. According to the principle of force interaction, tensile strain and compressive strain must occur at the same time. Thus, in GPA analysis, the areas with sharp changes in light and dark colors represent lattice distortions (marked by yellow arrows). By contrast, the pure FeOOH nanosheets sample without Ni content is also prepared through as-proposed oxygen-reduction deposition method, which suggests a similar morphology as Ni-FeOOH sample. The lattice fringes with a d-spacing of  $\sim 0.25$  nm can be attributed to the (101) plane of FeOOH (JCPDS card no. 99-0055). The diffraction ring in selected area electron diffraction (SAED) image (Fig. 2h) confirms the polycrystalline structure of FeOOH nanosheets. However, the area of dramatic change in tensile strain/compressive strain in Fig. 2i is obvious less than that in Fig. 2f, which suggest that Ni-FeOOH owns richer lattice distortion than FeOOH. Considering that the atomic radius of  $\text{Ni}^{2+}$  is larger than that of  $\text{Fe}^{3+}$ , the introduction of Ni content in FeOOH would cause extra lattice distortion. As has been reported by previous report [21,25], the stoichiometric number will change significantly at the distortions. The Ni or Fe atoms with unsaturated coordination near the distortion would be favorable for accepting oxygen-containing intermediate to balance the coordination, which is favorable for promoting the electrocatalytic water oxidation process.

### 3.3. The evidence of Ni cations existence in FeOOH lattice

The XRD pattern of Ni-FeOOH and FeOOH nanosheets in Fig. 3a can be ascribe to FeOOH crystal phases (JCPDS card No. 99-0055), where Ni doping does not change the phase of FeOOH. The exposed low-index facet is (110) plane, therefore, subsequent theoretical calculations are based on face (110) of the FeOOH phase. The introduce of Ni cation in FeOOH is expected to influence the bond length of surrounding coordination atoms. For further analysis, the pair distribution function (PDF) analysis is conducted, as shown in Fig. 3b. The first peak represents the shortest interaction distance of the atoms in the material, where the Ni-FeOOH nanosheets suggest a smaller interaction distance than FeOOH nanosheets. This is also consistent with the structural relaxation result by density functional theory (DFT) calculation, where the bond length of Ni-O pair ( $\sim 2.0 \text{ \AA}$ ) is obviously shorter than Fe-O pair ( $2.3 \text{ \AA}$ ). The shortage of atoms interaction distance would cause change in surface chemical states and electronic structure, which can be confirmed by X-ray photoelectron spectroscopy (XPS). The high-resolution Ni 2p XPS signal in Fig. 3c suggests a typical Ni 2p<sub>3/2</sub> peak at  $\sim 856.13 \text{ eV}$  in Ni-

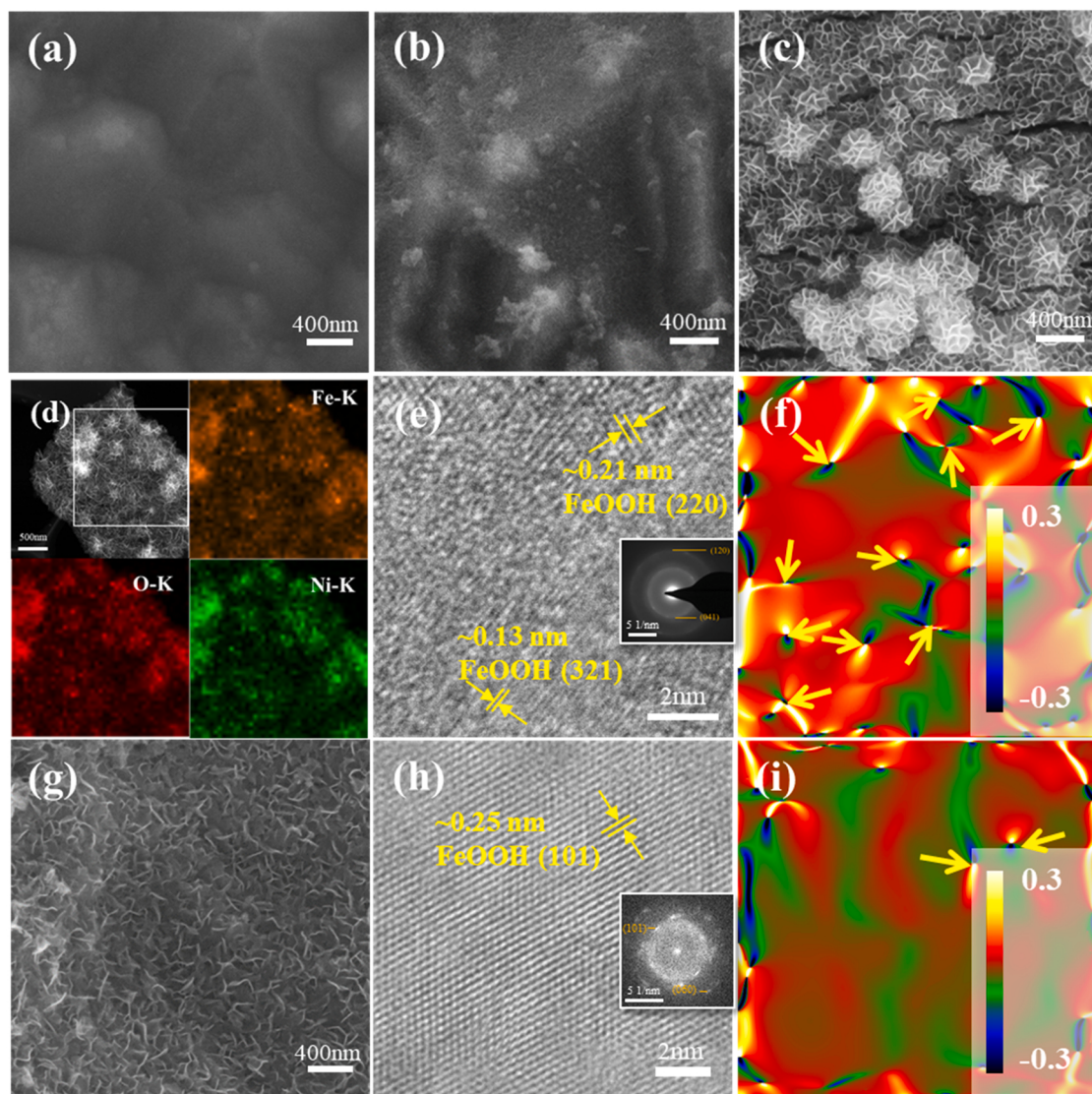


**Fig. 2.** The microstructure of (a) bare Fe network surface, (b) Fe-Soak sample and (c) Ni-FeOOH nanosheets derived by oxygen-reduction deposition. (d) The HADDF-STEM image of Ni-FeOOH nanosheets and corresponding elemental distribution of Fe, O and Ni. (e) The high-resolution TEM (HRTEM) image of Ni-FeOOH nanosheets, and the insert is selected area electron diffraction (SAED) images of Ni-FeOOH nanosheets. (f) The geometric phase analysis (GPA) along  $xx$  direction of Ni-FeOOH (the lattice distortions are marked by yellow arrow), (g) microstructure of FeOOH nanosheets, (h) HRTEM image of FeOOH nanosheets, (i) the geometric phase analysis (GPA) along  $xx$  direction of FeOOH.

FeOOH [26,27], which is  $\sim 0.6$  eV higher than Ni  $2p_{3/2}$  binding energy in standard NiOOH. This suggest that the average Ni valence is above  $+3$ . The Fe  $2p$  XPS spectra in Fig. 3d shows the typical Fe  $2p_{3/2}$  peaks at 711.33 eV, indicating the presence of Fe as  $Fe^{3+}$ . Importantly, the Fe  $2p_{3/2}$  peak of Ni-FeOOH ( $\sim 712.15$  eV) is positively shifted by 0.82 eV compared with FeOOH, which indicates a high average valence of Fe atoms between  $+3$  and  $+4$  [28]. The high Fe valence correlates with the rich holes in the valence band, which could benefit for accepting negatively charged intermediates such as  $OH^-$ ,  $OOH^-$ ,  $O^{2-}$  etc. Therefore, the OER electrocatalytic activity is expected to be facilitated. The O1s XPS signal of bare Fe network and Ni-FeOOH are respectively shown in Fig. 3c and Fig. 3d. The peaks in O 1s spectrum at 530.08 eV, 531.50 eV, 532.50 eV can be assigned to lattice  $O^{2-}$ , (oxy)hydroxyl group ( $^*OOH$ ), oxygen vacancies ( $O_v$ ), respectively [29–31]. The O 1s spectrum of FeOOH (Fig. 3e) suggests that there exists a main OOH composition, an equivalent content of lattice  $O^{2-}$ , and a minor content of oxygen vacancies ( $O_v$ ). In sharp contrast, the Ni-FeOOH suggests an obviously increased OOH composition and a dramatically decreased lattice  $O^{2-}$ , which confirms the Ni introduction benefits for increasing

oxidation degree and shifting average valence.

To give deeper insight of the Ni cation position in the lattice, based on (110) plane of FeOOH, the comparison among formation energies of interstitial sites and substitutive sites is conducted in Fig. 4. According to symmetry of geometric structure of surface, 2 kinds of interstitial Ni locations and 2 kinds of substitutive Ni locations can be modeled, as shown in Fig. 4a. It should be noted that there exist two kinds of substitutive locations: substituting Fe position and substituting H position. Corresponding formation energies are shown below in Fig. 4b, where the Ni-Substitutive site 1 model, e.g. substituting Fe position, suggests the lowest formation energy ( $-0.88$  eV). The negative energy value indicates the thermodynamically-tended formation process of such structure, which is considered to be the most stable and most probable structure of Ni-FeOOH nanosheets. Another evidence to support the Ni-substitutive location is the composition ratio of Ni-FeOOH and FeOOH measured by inductively coupled plasma (ICP) tests (Fig. S7). The FeOOH suggests a Fe content of  $\sim 27.3\%$  and an O content of  $72.7\%$ , while the Ni-FeOOH suggests a Fe content of  $\sim 20.1\%$ , a Ni content of  $\sim 7.9\%$  and an O content of  $72\%$ . The O content remains similar after Ni

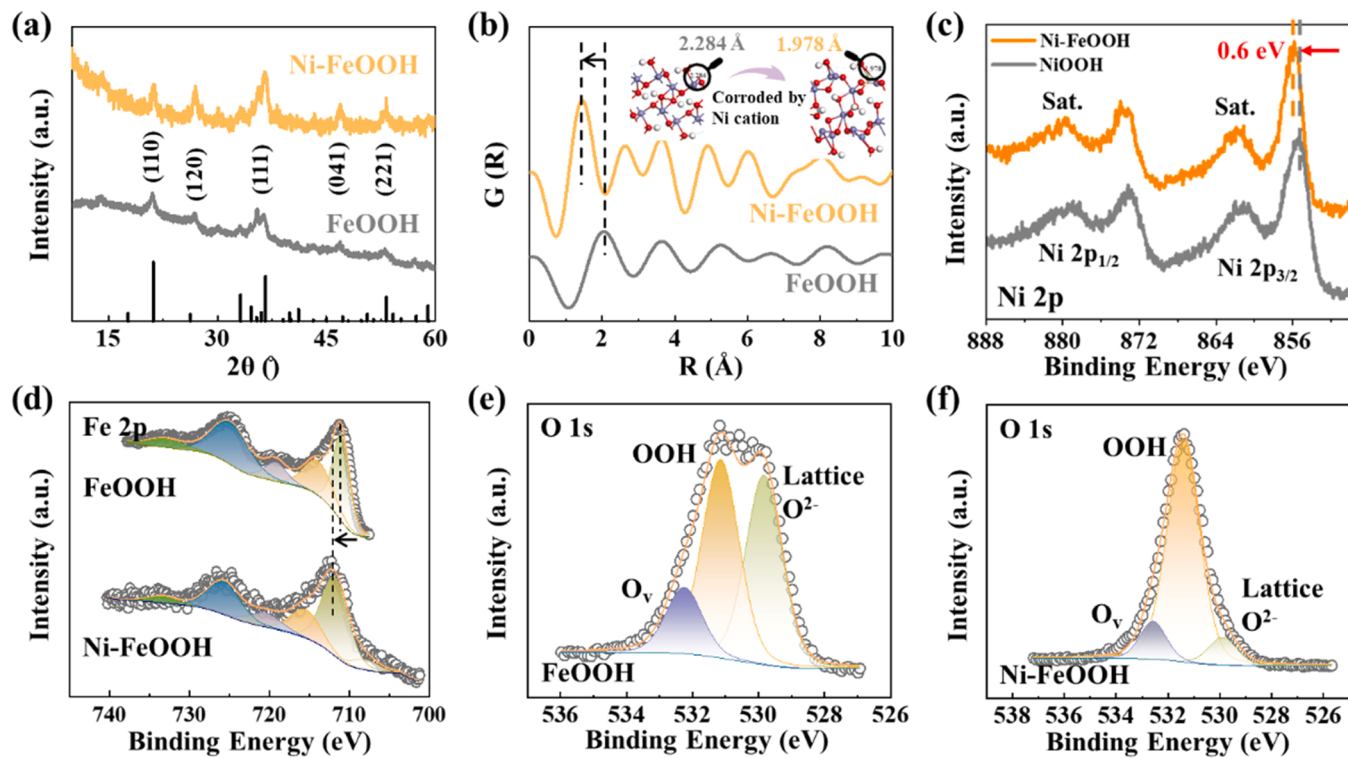


**Fig. 3.** (a) XRD patterns of FeOOH nanosheets and Ni-FeOOH nanosheets, (b) the pair distribution function (PDF) analysis for FeOOH nanosheets and Ni-FeOOH nanosheets, (c) the Ni 2p XPS spectra of standard NiOOH and Ni-FeOOH nanosheets, (d) Fe 2p XPS spectra of FeOOH nanosheets and Ni-FeOOH nanosheets, (e) O 1s XPS spectra of FeOOH nanosheets, (f) O 1s XPS spectra of Ni-FeOOH nanosheets.

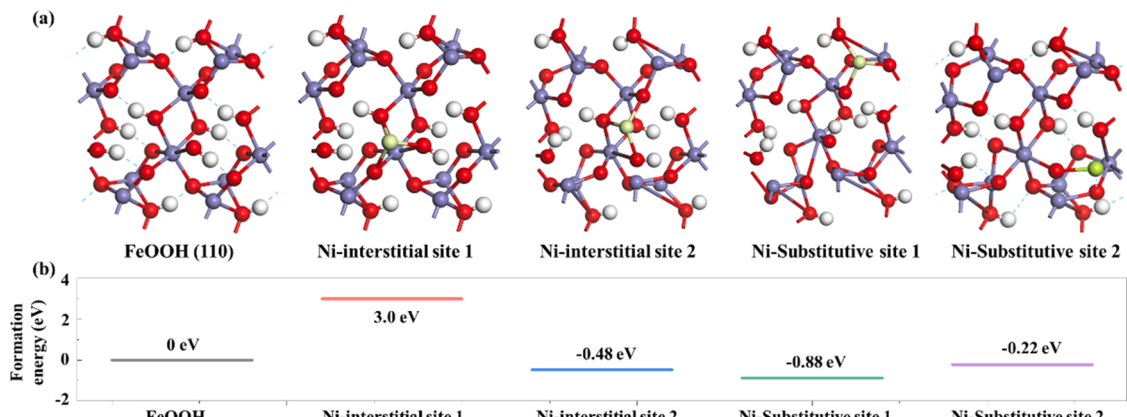


**Fig. 4.** (a) The atomic models of Ni-FeOOH with different Ni locations on (110) plane; (b) the formation energies calculation of different Ni locations in FeOOH lattice through density functional theory.

introduction, and the sum of Fe and Ni content in Ni-FeOOH is approximately equal to Fe content in FeOOH, which indicates that the Ni ions occupy the position of Fe ions in FeOOH lattice.

#### 3.4. The electrocatalytic water oxidation activities of as-prepared samples

The electrocatalytic OER performances of obtained samples are investigated in 1 M KOH, as shown in Fig. 5. The linear sweep voltammetry (LSV) curves of Ni-FeOOH nanosheets, FeOOH nanosheets, Fe-Soak sample and pristine Fe foam are shown in Fig. 5a. Ni-FeOOH nanosheets show the superior activity with the lowest overpotentials (239 mV at 10 mA/cm<sup>2</sup> and 264 mV at 50 mA/cm<sup>2</sup>) among FeOOH (295 mV at 10 mA/cm<sup>2</sup> and 353 mV at 50 mA/cm<sup>2</sup>), Fe-Soak (306 mV at 10 mA/cm<sup>2</sup> and 366 mV at 50 mA/cm<sup>2</sup>) and pristine Fe foam

(357 mV at 10 mA/cm<sup>2</sup> and 411 mV at 50 mA/cm<sup>2</sup>), as shown in Fig. 5b. To further understand the OER kinetics, the Tafel plots are calculated in Fig. 5c. Ni-FeOOH shows the smallest Tafel slope of  $\sim 33$  mV dec<sup>-1</sup>, which is much smaller than that of pristine Fe foam (69 mV dec<sup>-1</sup>) and Fe-Soak (70 mV dec<sup>-1</sup>), suggesting the greatly facilitated rate-determining step for Ni-FeOOH nanosheets. Meanwhile, electrochemical impedance spectroscopy (EIS) results in Fig. 5d also show a more favorable kinetics of Ni-FeOOH with an obviously smaller arc radius, suggesting the decrease of the charge transfer resistance ( $R_{ct}$ ) of Ni-FeOOH at the electrochemical reaction interface [32–34]. It should be noted that the overpotential of IrO<sub>2</sub> contrast sample at 10 mA/cm<sup>2</sup> is 220 mV, which is  $\sim 19$  mV lower than that of Ni-FeOOH sample. However, while the current density reaches above 100 mA/cm<sup>2</sup>, the Ni-FeOOH owns obviously smaller overpotential than commercial IrO<sub>2</sub>

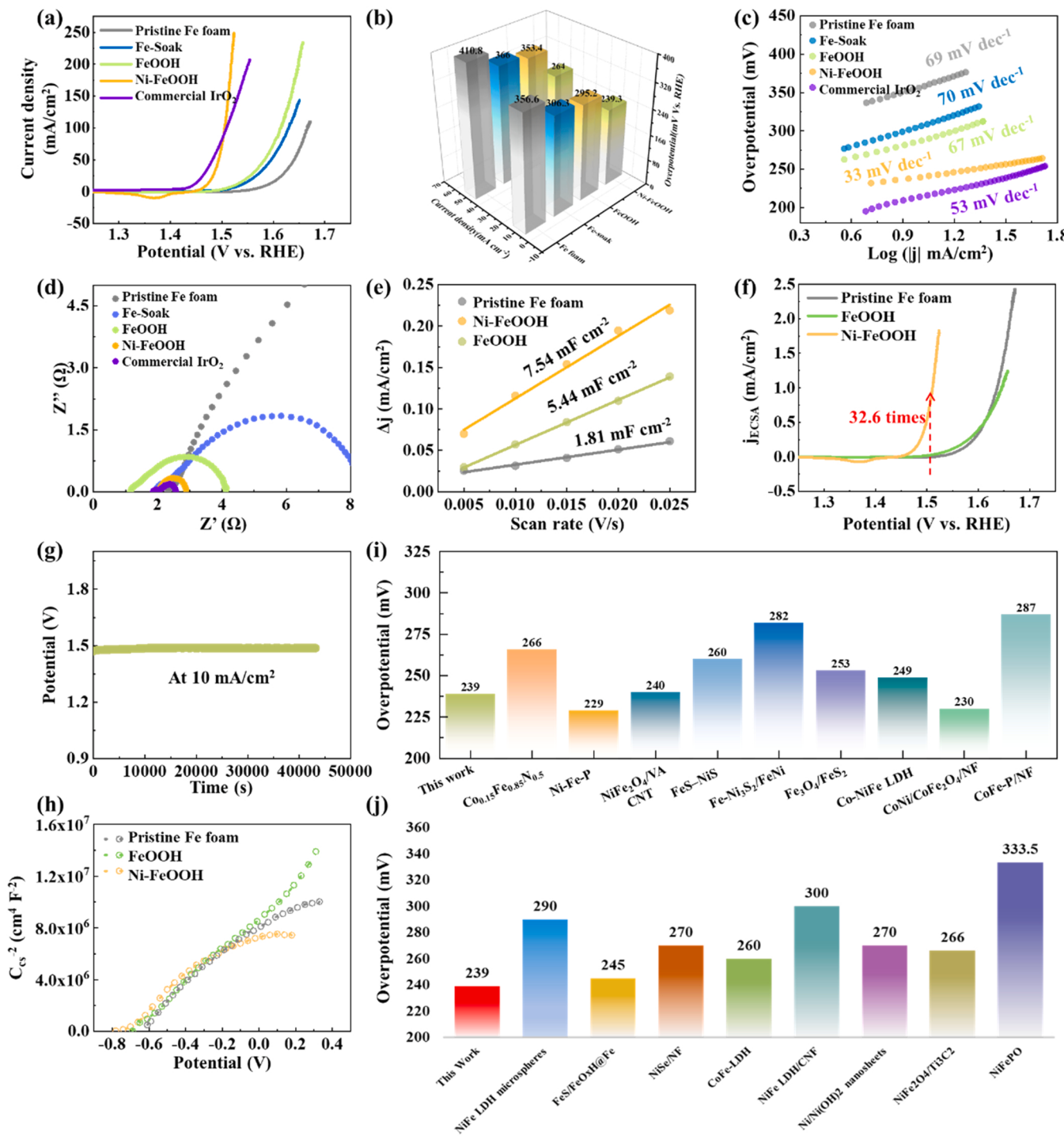


**Fig. 5.** The (a) polarization curves, (b) statics of overpotentials under 10 mA/cm<sup>2</sup> and 50 mA/cm<sup>2</sup>, (c) Tafel plots, (d) Nyquist plots, (e) the fitted double layer capacitor ( $C_{dl}$ ) values for estimating electrochemical specific area (ECSA), (f) the polarization curves standardized by ECSA, (g) the Chronopotentiometric curve of Ni-FeOOH, (h) the Mott-Schottky tests, (i, j) performances comparison among Ni-FeOOH and other similar electrocatalysts.

(Fig. 5a). The Ni-FeOOH and commercial  $\text{IrO}_2$  own a similar charge transferring resistance (Fig. 5d), however, the Ni-FeOOH owns a smaller Tafel slope ( $\sim 33 \text{ mV dec}^{-1}$ ) than commercial  $\text{IrO}_2$  ( $53 \text{ mV dec}^{-1}$ ) under the same current density range, which indicates a better catalytic kinetics of as-prepared Ni-FeOOH nanosheets (Fig. 5c).

The electrochemical specific area (ECSA) is estimated through cyclic voltammetry (CV) curves tested at non-Faraday potential area (Fig. S8), and the double layer capacitor is positively correlated with ECSA. The Ni-FeOOH suggests the largest ECSA ( $7.54 \text{ mF/cm}^2$ ) among FeOOH

( $5.44 \text{ mF/cm}^2$ ) and pristine Fe foam ( $1.81 \text{ mF/cm}^2$ ), which demonstrated the increased active sites induced by Ni introduction (Fig. 5e). Further, the polarization curves are standardized by ECSA in Fig. 5f for estimating the intrinsic activity, which is in direct proportion to turnover frequency (TOF). The Ni-FeOOH suggests a  $j_{ECSA}$  32.6 times higher than FeOOH, which confirms that the Ni introduction not only increases the active sites, but also increases the intrinsic activity. The steady Chronopotentiometric curve below 1.5 V in Fig. 5g suggests the robust catalytic process of Ni-FeOOH. The Mott-Schottky curves tested near the

open-circuit potential are shown in Fig. 5h, where the positive slope suggests characteristics of hole as carrier on catalysts surface. It should be noted that the surface of pristine Fe foam would be naturally oxidized into Fe-oxides, which suggests a p-type semiconductor characteristic. The Ni-FeOOH suggests a lower slope than FeOOH, which confirms that the Ni introduction benefits for increasing carriers density. Importantly, current method can be easily applied for large-area electrodes fast preparation. The electrode area that can be prepared at one time has been expanded hundreds of times within short cycle of 20 min. Besides, after long-term stability test, the nanosheets morphology remains stable, further proving the robustness of as proposed oxygen-reduction methods (Fig. S9). The Ni-FeOOH derived by as-proposed method surpasses most mainstream electrocatalysts composed of similar materials system (Fig. 5i and Fig. 5j) [35–50], which confirms the bright potential for scaled-up application in green and economic production of self-support electrocatalysts.

### 3.5. The decrease of electrons momentum change and facilitation of transfer process

To further figure out the mechanism of catalytic performance enhancement, the electronic structure properties are calculated in Figs 6 and 7. The work function of FeOOH and Ni-FeOOH slabs is revealed through electrostatic potential distribution along Z direction (Figs. 6a and 6b), where the Ni-FeOOH suggests a larger work function (0.184 Ha) than FeOOH (0.179 Ha). Taking vacuum energy level as standard, the Fermi level of Ni-FeOOH is downshifted after Ni introduction, which is beneficial for accepting electrons from KOH solution through catalyst-electrolyte interface. The high resolution ultraviolet

photoelectron spectrometer (UPS) is further used to verify the calculation. Fig. S10 suggests that Ni-FeOOH (~3.66 eV) owns an obviously larger work function than FeOOH (~3.58 eV), which is consistent with the calculated results in Figs. 6a and 6b. The isosurface of atomic deformation electron density distribution is calculated in Fig. 6d to illustrate the reasons of high-valence Ni and Fe atoms in Ni-FeOOH. The red area and blue area represent the surrounding electrons decreasing and increasing induced by Ni coupling respectively. During synthetic process, in the liquid layer, due to that the redox potential of  $O_2$  ( $\psi = 1.23$  V) is much higher than those of  $Fe^{2+}$  ( $\psi = 0.77$  V) and  $Ni^{2+}$  ( $\psi = 0.49$  V), the  $Ni^{2+}$  and  $Fe^{2+}$  (if any) would be oxidized to +3 or higher valence by dissolved oxygen. Electronegativity difference exists between  $Fe^{3+}$  and  $Ni^{3+}$ , therefore, some electrons would be delocalized due to the electronic interaction. Fig. 6d suggests that the electrons around the Ni and Fe centers decrease, while the electrons around the O centers increase. Compared with FeOOH, the Ni coupling in Ni-FeOOH caused some electrons delocalizing from Ni/Fe centers to O centers. Thus, the average valence of Ni, Fe atoms becomes higher, which is consistent with XPS analysis in Fig. 3. Further, the total electron density distribution of FeOOH (Fig. 6e) and Ni-FeOOH (Fig. 6f) also confirms the decreased electrons distribution near Ni heteroatoms (marked by red arrows), which benefits for forming hole channel to accept electrons from electrolyte. On the other hand, the electrons acceptor behavior is also affected by electrons momentum change. The FeOOH suggests a typical indirect band gap with the electrons reflection  $O\rightarrow\alpha$ , while the Ni-FeOOH suggests a state similar to direct band gap with the electrons reflection  $O\rightarrow\beta$ . The shortened reflection from  $O\alpha$  to  $O\beta$  indicates a smaller electrons momentum change during electrocatalyst-electrolyte interfacial charge transfer, which confirms that the Ni introduction

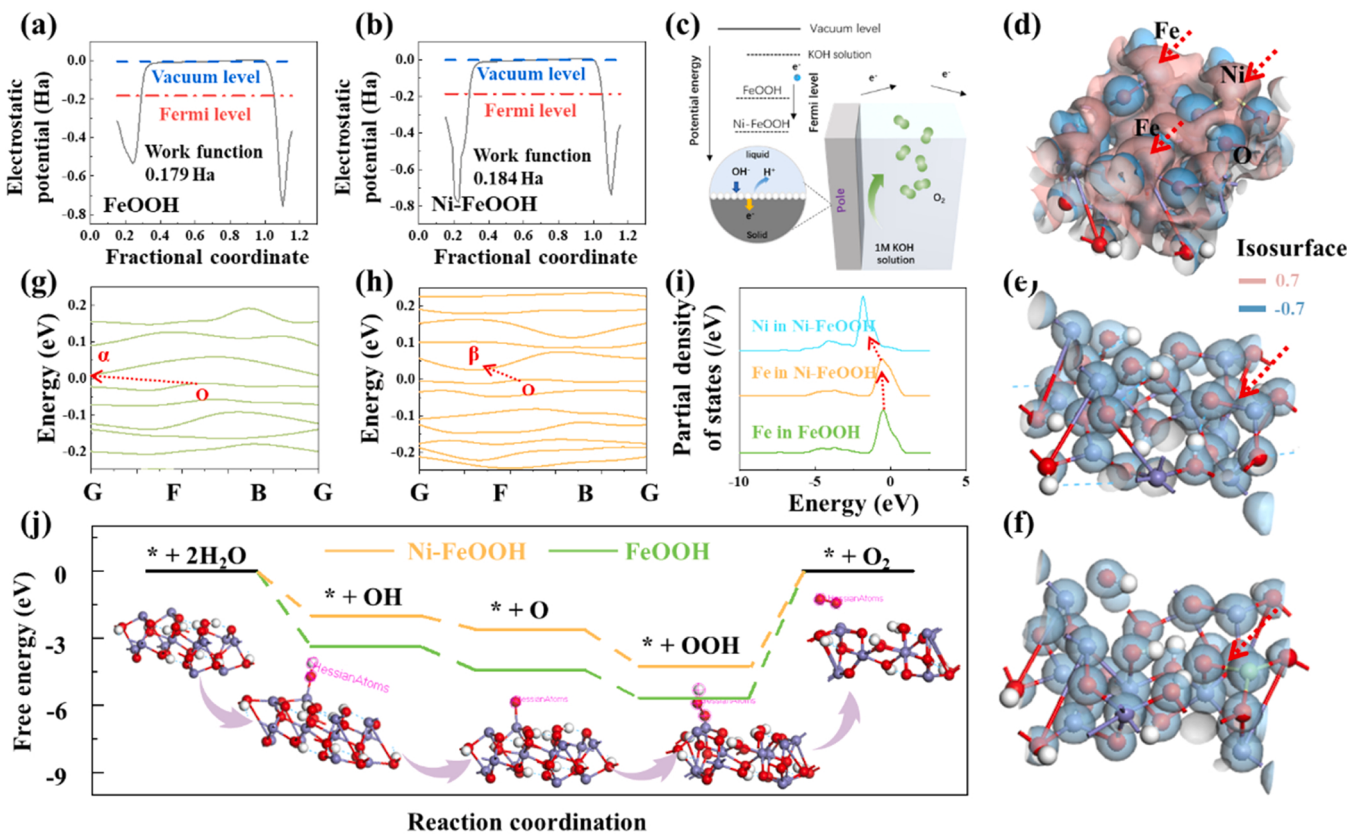


**Fig. 6.** The electrostatic potential distribution of (a) FeOOH nanosheets and (b) Ni-FeOOH nanosheets along Z direction, (c) the illustration of acceptor behaviors, (d) the isosurface of atomic deformation electron density distribution of Ni-FeOOH, the red arrow marks the delocalized charge after Ni introduction; the isosurface of total electron density distribution of (e) FeOOH and (f) Ni-FeOOH; the electronic energy band structure of (g) FeOOH and (h) Ni-FeOOH; (i) the partial density of states (PDOS) of Fe sites in FeOOH and Fe, Ni sites in Ni-FeOOH, (j) the step diagram of adsorption free energy change of intermediates on Fe sites in FeOOH and Ni-FeOOH.

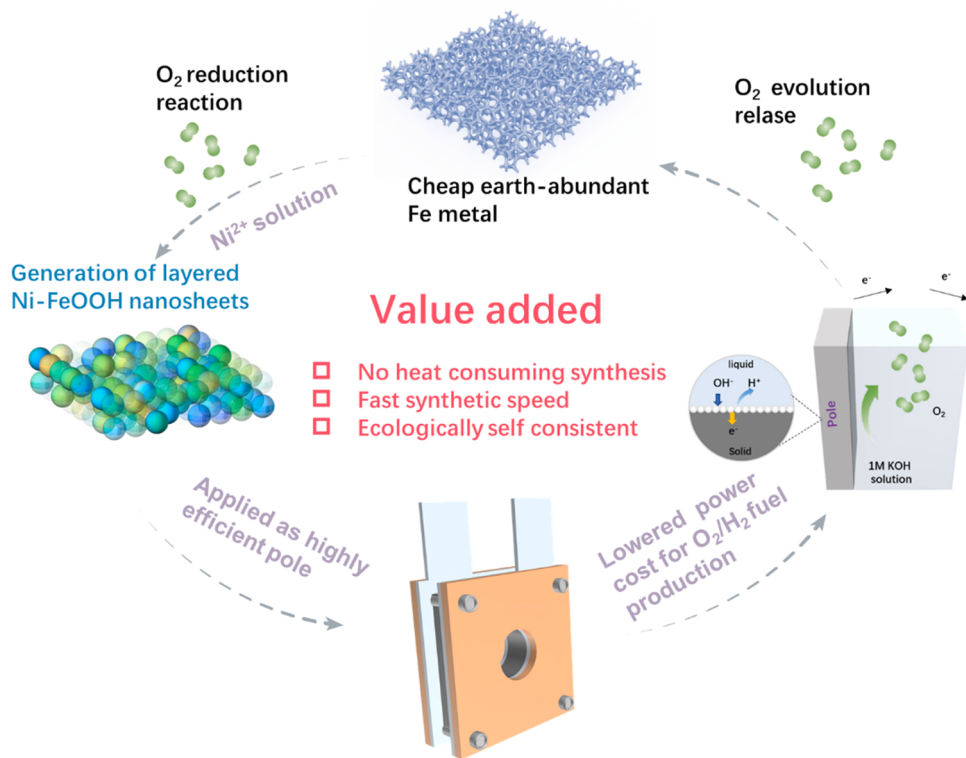


**Fig. 7.** The schematic illustration of economic and ecological attributes of as-proposed oxygen-reduction deposition method.

decreased the charge transfer resistance. This is also corresponding with the EIS analysis in Fig. 5d. The partial density of states shown in Fig. 6i reveals that after Ni introduction, both the Fe site and Ni site show the decreased energy band center, which is consistent with the average valence increase in XPS analysis (Fig. 3) and the increase of hole carrier (Fig. 5h). The Ni in Ni-FeOOH owns a lower band center than Fe in Ni-FeOOH, which can be attributed to that the ionic radius of Ni is  $\sim 0.005$  nm larger than that of Fe. According to the formation energies calculation in Fig. 4, the Ni cations tend to replace Fe sites in FeOOH. After occupancy, the bands of Ni center would be compressed and overlapped by surrounding coordinating atoms. Therefore, the Ni in Ni-FeOOH will suggest a lower band center than Fe in Ni-FeOOH. The step-diagram of adsorption free energy on Ni sites in Ni-FeOOH is also calculated in Fig. S11, where the energy barrier of RDS is lower than that of FeOOH by  $\sim 1.37$  eV. The largest energy barrier emerges at the same step ( $^* + \text{OOH} - \text{e}^- \rightarrow ^* + \text{O}_2 + \text{H}^+$ ) on both Ni and Fe sites, and the energy barriers are similar (Fig. S12). Therefore, both Fe atoms and Ni atoms can serve as active sites during OER process. To be exact, the reaction energy barrier on Fe sites is  $\sim 0.03$  eV lower than that on Ni sites, which means that the Fe sites are favorable for OER and believed to be main active sites. As a result, the energy barrier of the rate-determining step (RDS) on Fe sites in Ni-FeOOH surface is lowered by  $\sim 1.4$  eV, which confirms that Ni introduction greatly modifies the electronic structures of Fe sites.

In brief, based on experimental results and DFT calculation, both Ni and Fe atoms participate in OER, and Fe atoms are the main active sites. The Ni atoms in Ni-FeOOH play a role of enhancing the activities of Fe sites.

### 3.6. The ecological and economic properties of ORD method

Briefly, as proposed oxygen-reduction deposition method suggests bright potential for value added electrocatalysts. Three aspects should be emphasized: (1) Current method can achieve no heat consuming synthesis. The driving force of synthesis process comes from the REDOX

potential difference between Fe metal substrates and dissolved oxygen at room temperature, which requires no additional heat input. (2) Fast synthetic speed. A single oxygen-reduction deposition process only takes 20 min. (3) Ecologically self-consistent. The main ingredient is Fe metal, which is one of the metals with the highest crustal abundance [51,52]. Through consuming oxygen in the atmosphere, highly active Ni-FeOOH nanosheets are in-situ generated, which is favorable for serving as electrocatalyst to generate  $\text{O}_2$  with low power cost. The produced  $\text{O}_2$  can be used in various practical scenarios, such as engineering manufacturing, aerospace, medical and other fields, and can also be discharged into the atmosphere without pollution. The oxygen in the atmosphere can be used for continuous production in the next cycle, which realizes ecological self-consistency.

### 3.7. The potential application scenarios of as-prepared Ni-FeOOH electrocatalysts

The potential application scenarios include but are not limited to the following aspects. (1) The electrodes in electrolyzer to produce hydrogen. The hydrogen produced through electrocatalytic water splitting has attracted more and more interests from academia to industry, due to the great potential of waste electricity utilization and carbon emissions reduction. Current Ni-FeOOH can serve as anodes to lower the overall voltage for water splitting electrolyzers. (2) The anodes in electrolyzer to reduce  $\text{CO}_2$ . The carbon neutralization has become a common concern for the whole world. Besides the  $\text{CO}_2$  reduction reaction occurring in cathode, the  $\text{CO}_2$  electrolyzer contains another half-reaction which is usually oxygen evolution reaction (OER). Current Ni-FeOOH electrocatalysts can serve as anodes to lower the cell voltage for electrocatalytic  $\text{CO}_2$  reduction. Since current method owns advantage of scaled-up preparation, the Ni-FeOOH electrodes of a series of sizes can be achieved conveniently within 20 min, which further opens up the applicability to different types of electrolyzers.

#### 4. Conclusion

An oxygen-reduction deposition method is proposed for fast in-situ generation of Ni incorporated FeOOH nanosheets on Fe network surface at room temperature atmosphere. The driving force of synthesis originates from the natural REDOX potential difference between dissolved O<sub>2</sub> and Fe substrate. The Ni heteroatoms introduction (~7 a.t.%) on FeOOH surface shifts the Fe average valence to above + 3, which decreases Fermi level and increases electron acceptor. As a result, energy barrier of rate-determining step on both Ni sites and Fe sites is reduced compared with pure FeOOH, which results in an OER activity in alkaline media with small Tafel slope of 33 mV/dec and an overpotential of 239 mV at 10 mA/cm<sup>2</sup>. Current method affords unique advantages of large-scale nano-electrocatalysts with short synthetic period (~20 min) and ultralow synthetic costs (no requirement for high temperature/pressure and noble ingredients), which owns potential as fast platform for studying and producing cost-effective Fe-based electrocatalysts featuring industrial scenarios.

#### CRediT authorship contribution statement

**Yaotian Yan:** Investigation, Data curation, Formal analysis, Writing – original draft. **Keke Huang:** Conceptualization, Formal analysis. **Jinghuang Lin:** Formal analysis. **Taili Yang:** Investigation, Data curation. **Peijia Wang:** Writing – review & editing. **Liang Qiao:** DFT calculation. **Wei Cai:** Resources. **Xiaohang Zheng:** Investigation, Data curation, Formal analysis, Funding acquisition.

#### Declaration of Competing Interest

The authors declare that they have no known competing financial interests or personal relationships that could have appeared to influence the work reported in this paper.

#### Data Availability

Data will be made available on request.

#### Acknowledgements

The support from the National Natural Science Foundation of China (No. 51971083) is highly appreciated. This work was also supported by Heilongjiang Touyan Innovation Team Program.

#### Appendix A. Supporting information

Supplementary data associated with this article can be found in the online version at [doi:10.1016/j.apcatb.2023.122595](https://doi.org/10.1016/j.apcatb.2023.122595).

#### References

- Z.F. Huang, J.J. Song, Y.H. Du, S.B. Xi, S. Dou, J.M.V. Nsanzimana, C. Wang, Z.C. J. Xu, X. Wang, Chemical and structural origin of lattice oxygen oxidation in Co-Zn oxyhydroxide oxygen evolution electrocatalysts, *Nat. Energy* 4 (2019) 329–338, <https://doi.org/10.1038/s41560-019-0355-9>.
- Z.J. Zhu, H.J. Yin, Y. Wang, C.H. Chuang, L. Xing, M.Y. Dong, Y.R. Lu, G. Casillas-Garcia, Y.L. Zheng, S. Chen, Y.H. Dou, P. Liu, Q.L. Cheng, H.J. Zhao, Coexisting single-atomic Fe and Ni sites on hierarchically ordered porous carbon as a highly efficient ORR electrocatalyst, *Adv. Mater.* 32 (2020) 2004670, <https://doi.org/10.1002/adma.202004670>.
- J.J. Song, C. Wei, Z.F. Huang, C.T. Liu, L. Zeng, X. Wang, Z.C.J. Xu, A review on fundamentals for designing oxygen evolution electrocatalysts, *Chem. Soc. Rev.* 49 (2020) 2196–2214, <https://doi.org/10.1039/c9cs00607a>.
- X.B. Zhu, B. Hu, C.X. Wang, X.H. An, J.L. He, X.B. Wang, Y. Zhao, Self-assembly induced metal ionic-polymer derived Fe-N-x/C nanowire as oxygen reduction reaction electrocatalyst, *J. Catal.* 391 (2020) 1–10, <https://doi.org/10.1016/j.jcat.2020.08.016>.
- Y.T. Yan, J.H. Lin, T.X. Xu, B.S. Liu, K.K. Huang, L. Qiao, S.D. Liu, J. Cao, S.C. Jun, Y. Yamauchi, J.L. Qi, Atomic-level platinum filling into Ni-vacancies of dual-deficient NiO for boosting electrocatalytic hydrogen evolution, *Adv. Energy Mater.* 12 (2022) 2200434, <https://doi.org/10.1002/aenm.202200434>.
- N.T. Suen, S.F. Hung, Q. Quan, N. Zhang, Y.J. Xu, H.M. Chen, Electrocatalysis for the oxygen evolution reaction: recent development and future perspectives, *Chem. Soc. Rev.* 46 (2017) 337–365, <https://doi.org/10.1039/c6cs00328a>.
- Y.L. Pan, X.M. Xu, Y.J. Zhong, L. Ge, Y.B. Chen, J.P.M. Veder, D.Q. Guan, R. O'Hare, M.R. Li, G.X. Wang, H. Wang, W. Zhou, Z.P. Shao, Direct evidence of boosted oxygen evolution over perovskite by enhanced lattice oxygen participation, *Nat. Commun.* 11 (2020) 2002, <https://doi.org/10.1038/s41467-020-15873-x>.
- X.P. Wang, H.J. Wu, S.B. Xi, W.S.V. Lee, J. Zhang, Z.H. Wu, J.O. Wang, T.D. Hu, L. M. Liu, Y. Han, S.W. Chee, S.C. Ning, U. Mirsaidov, Z.B. Wang, Y.W. Zhang, A. Borgna, J. Wang, Y.H. Du, Z.G. Yu, S.J. Pennycook, J.M. Xue, Strain stabilized nickel hydroxide nanoribbons for efficient water splitting, *Energ. Environ. Sci.* 13 (2020) 229–237, <https://doi.org/10.1039/c9ee02565k>.
- Y.T. Yan, P.C. Wang, J.H. Lin, J. Cao, J.L. Qi, Modification strategies on transition metal-based electrocatalysts for efficient water splitting, *J. Energy Chem.* 58 (2021) 446–462, <https://doi.org/10.1016/j.jec.2020.10.0102095-4956>.
- Y.T. Yan, J.H. Lin, J. Cao, S. Guo, X.H. Zheng, J.C. Feng, J.L. Qi, Activating and optimizing the activity of NiCoP nanosheets for electrocatalytic alkaline water splitting through the V doping effect enhanced by P vacancies, *J. Mater. Chem. A* 7 (2019) 24486–24492, <https://doi.org/10.1039/c9ta09283h>.
- D. Friebel, M.W. Louie, M. Bajdich, K.E. Sanwald, Y. Cai, A.M. Wise, M.J. Cheng, D. Sokaras, T.C. Weng, R. Alonso-Mori, R.C. Davis, J.R. Bargar, J.K. Norskov, A. Nilsson, A.T. Bell, Identification of highly active Fe sites in (Ni,Fe)OOH for electrocatalytic water splitting, *J. Am. Chem. Soc.* 137 (2015) 1305–1313, <https://doi.org/10.1021/ja511559d>.
- J.L. Qi, Y.T. Yan, Y.F. Cai, J. Cao, J.C. Feng, Nanoarchitected design of vertical-standing arrays for supercapacitors: progress, challenges, and perspectives, *Adv. Funct. Mater.* 31 (2021) 2006030, <https://doi.org/10.1002/adfm.202006030>.
- Y. Yan, J. Liu, K. Huang, J. Qi, L. Qiao, X. Zheng, W. Cai, A fast micro-nano liquid layer induced construction of scaled-up oxyhydroxide based electrocatalysts for alkaline water splitting, *J. Mater. Chem. A* 9 (2021) 26777–26787, <https://doi.org/10.1039/DTA07972G>.
- J. Yu, J. Wang, X. Long, L. Chen, Q. Cao, J. Wang, C. Qiu, J. Lim, S.H. Yang, Formation of FeOOH nanosheets induces substitutional doping of CeO<sub>2-x</sub> with high-valence Ni for efficient water oxidation, *Adv. Energy Mater.* 11 (2021) 2002731, <https://doi.org/10.1002/aenm.202002731>.
- W. Adamson, X. Bo, Y.B. Li, B.H.R. Suryanto, X.J. Chen, C. Zhao, Co-Fe binary metal oxide electrocatalyst with synergistic interface structures for efficient overall water splitting, *Catal. Today* 351 (2020) 44–49, <https://doi.org/10.1016/j.cattod.2019.01.060>.
- X.Q. Du, H. Su, X.S. Zhang, Metal-organic framework-derived M (M = Fe, Ni, Zn and Mo) doped Co<sub>9</sub>S<sub>8</sub> nanoarrays as efficient electrocatalyst for water splitting: the combination of theoretical calculation and experiment, *J. Catal.* 383 (2020) 103–116, <https://doi.org/10.1016/j.jcat.2020.01.015>.
- Q.L. Han, X.M. Zhao, Y.H. Luo, L.L. Wu, S.J. Sun, J.D. Li, Y.J. Wang, G.H. Liu, Z. W. Chen, Synergistic binary Fe-Co nanocluster supported on defective tungsten oxide as efficient oxygen reduction electrocatalyst in zinc-air battery, *Adv. Sci.* 9 (2022) 2104237, <https://doi.org/10.1002/advs.202104237>.
- W.J. Zhang, K.C. Fan, C.H. Chuang, P.R. Liu, J. Zhao, D.C. Qi, L.B. Zong, L. Wang, Molten salt assisted fabrication of Fe@Fe-SA-N-C oxygen electrocatalyst for high performance Zn-air battery, *J. Energy Chem.* 61 (2021) 612–621, <https://doi.org/10.1016/j.jec.2021.02.0152095-4956>.
- C.C. Weng, X.W. Lv, J.T. Ren, T.Y. Ma, Z.Y. Yuan, Engineering gas-solid-liquid triple-phase interfaces for electrochemical energy conversion reactions, *Electrochim. Energy Rev.* 5 (2022) 19, <https://doi.org/10.1007/s41918-022-00133-x>.
- B.M. Hunter, N.B. Thompson, A.M. Muller, G.R. Rossman, M.G. Hill, J.R. Winkler, H.B. Gray, Trapping an Iron(VI) water-splitting intermediate in nonaqueous media, *Joule* 2 (2018) 747–763, <https://doi.org/10.1016/j.joule.2018.01.008>.
- J.D. Chen, F. Zheng, S.J. Zhang, A. Fisher, Y. Zhou, Z.Y. Wang, Y.Y. Li, B.B. Xu, J. T. Li, S.G. Sun, Interfacial interaction between FeOOH and Ni-Fe LDH to modulate the local electronic structure for enhanced OER electrocatalysis, *ACS Catal.* 8 (2018) 11342–11351, <https://doi.org/10.1021/acscatal.8b03489>.
- H.T. Lu, M.H. Sui, B.J. Yuan, J.Y. Wang, Y.N. Lv, Efficient degradation of nitrobenzene by Cu-Co-Fe-LDH catalyzed peroxymonosulfate to produce hydroxyl radicals, *Chem. Eng. J.* 357 (2019) 140–149, <https://doi.org/10.1016/j.cej.2018.09.111>.
- H.T. Lu, Z.L. Zhu, H. Zhang, J.Y. Zhu, Y.L. Qiu, L.Y. Zhu, S. Kuppers, Fenton-like catalysis and oxidation/adsorption performances of acetaminophen and arsenic pollutants in water on a multimetall Cu-Zn Fe-LDH, *ACS Appl. Mater. Interfaces* 8 (2016) 25343–25352, <https://doi.org/10.1021/acsami.6b08933>.
- Q.Q. Zhao, S.J. Geng, Y. Zhang, G. Chen, S.L. Zhu, F.H. Wang, High-entropy FeCoNiMnCu alloy coating on ferritic stainless steel for solid oxide fuel cell interconnects, *J. Alloy Compd.* 908 (2022), 164608, <https://doi.org/10.1016/j.jallcom.2022.164608>.
- S.C. Du, Z.Y. Ren, X.L. Wang, J. Wu, H.Y. Meng, H.G. Fu, Controlled atmosphere corrosion engineering toward Inhomogeneous NiFe-LDH for energetic oxygen evolution, *ACS Nano* 16 (2022) 7794–7803, <https://doi.org/10.1021/acsnano.2c00332>.
- J.H. Lin, P.C. Wang, H.H. Wang, C. Li, X.Q. Si, J.L. Qi, J. Cao, Z.X. Zhong, W.D. Fei, J.C. Feng, Defect-rich heterogeneous MoS<sub>2</sub>/NiS<sub>2</sub> nanosheets electrocatalysts for efficient overall water splitting, *Adv. Sci.* 6 (2019) 1900246, <https://doi.org/10.1002/advs.201900246>.

[27] H.F. Fan, W. Chen, G.L. Chen, J. Huang, C.S. Song, Y. Du, C.R. Li, K. Ostrikov, Plasma-heteroatom-doped Ni-V-Fe trimetallic phospho-nitride as high-performance bifunctional electrocatalyst, *Appl. Catal. B-Environ.* 268 (2020), 118440, <https://doi.org/10.1016/j.apcatb.2019.118440>.

[28] S. Cheng, C. Shen, H. Zheng, F.Q. Liu, A.M. Li, OCNTs encapsulating Fe-Co PBA as efficient chainmail-like electrocatalyst for enhanced heterogeneous electro-Fenton reaction, *Appl. Catal. B-Environ.* 269 (2020), 118785, <https://doi.org/10.1016/j.apcatb.2020.118785>.

[29] H.N. Jia, Z.Y. Wang, C. Li, X.Q. Si, X.H. Zheng, Y.F. Cai, J.H. Lin, H.Y. Liang, J. L. Qi, J. Cao, J.C. Feng, W.D. Fei, Designing oxygen bonding between reduced graphene oxide and multishelled  $Mn_3O_4$  hollow spheres for enhanced performance of supercapacitors, *J. Mater. Chem. A* 7 (2019) 6686–6694, <https://doi.org/10.1039/c8ta11482j>.

[30] X.S. Wang, Y.Y. Pan, H. Ning, H.M. Wang, D.L. Guo, W.H. Wang, Z.X. Yang, Q. S. Zhao, B.X. Zhang, L.R. Zheng, J.L. Zhang, M.B. Wu, Hierarchically micro- and meso-porous  $Fe-N_4O$ -doped carbon as robust electrocatalyst for  $CO_2$  reduction, *Appl. Catal. B-Environ.* 266 (2020), 118630, <https://doi.org/10.1016/j.apcatb.2020.118630>.

[31] X. Tan, X. Liu, Y.Y. Si, Z.H. Lv, Z.H. Li, G.X. Wang, G.W. Xie, Electrodeposited  $Ni-Fe-P/FeMnO_3/Fe$  multi-stage nanostructured electrocatalyst with superior catalytic performance for water splitting, *J. Mater. Chem. A* 9 (2021) 21101–21110, <https://doi.org/10.1039/dta04518k>.

[32] Y.T. Yan, J.H. Lin, T. Liu, B.S. Liu, B. Wang, L. Qiao, J.C. Tu, J. Cao, J.L. Qi, Corrosion behavior of stainless steel-tungsten carbide joints brazed with  $AgCuX$  ( $X = In, Ti$ ) alloys, *Corros. Sci.* 200 (2022), 110231, <https://doi.org/10.1016/j.jcsc.2022.110231>.

[33] H.N. Jia, Y.F. Cai, J.H. Lin, H.Y. Liang, J.L. Qi, J. Cao, J.C. Feng, W.D. Fei, Heterostructured graphene quantum dot/ $MnO_2$  nanosheets toward high-potential window electrodes for high-performance supercapacitors, *Adv. Sci.* 5 (2018) 1700887, <https://doi.org/10.1002/advs.201700887>.

[34] H.A. Jia, Z.Y. Wang, X.H. Zheng, J.H. Lin, H.Y. Liang, Y.F. Cai, J.L. Qi, J. Cao, J. C. Feng, W.D. Fei, Interlaced Ni-Co LDH nanosheets wrapped  $Co_9S_8$  nanotube with hierarchical structure toward high performance supercapacitors, *Chem. Eng. J.* 351 (2018) 348–355, <https://doi.org/10.1016/j.cej.2018.06.113>.

[35] L. An, J.R. Feng, Y. Zhang, Y.Q. Zhao, R. Si, G.C. Wang, F.Y. Cheng, P.X. Xi, S. H. Sun, Controllable tuning of Fe-N nanosheets by Co substitution for enhanced oxygen evolution reaction, *Nano Energy* 57 (2019) 644–652, <https://doi.org/10.1016/j.nanoen.2018.12.094>.

[36] D.H. Duan, D.S. Guo, J. Gao, S.B. Liu, Y.F. Wang, Electrodeposition of cobalt-iron bimetal phosphide on Ni foam as a bifunctional electrocatalyst for efficient overall water splitting, *J. Colloid Interface Sci.* 622 (2022) 250–260, <https://doi.org/10.1016/j.jcis.2022.04.127>.

[37] S.S. Li, S. Sirisomboonchai, A. Yoshida, X.W. An, X.G. Hao, A. Abudula, G.Q. Guan, Bifunctional CoNi/Co $Fe_2O_4$ /Ni foam electrodes for efficient overall water splitting at a high current density, *J. Mater. Chem. A* 6 (2018) 19221–19230, <https://doi.org/10.1039/c8ta08223e>.

[38] X.Q. Luan, H.T. Du, Y. Kong, F.L. Qu, L.M. Lu, A novel FeS-NiS hybrid nanoarray: an efficient and durable electrocatalyst for alkaline water oxidation, *Chem. Commun.* 55 (2019) 7335–7338, <https://doi.org/10.1039/c9cc02007a>.

[39] C.Z. Yuan, Z.T. Sun, Y.F. Jiang, Z.K. Yang, N. Jiang, Z.W. Zhao, U.Y. Qazi, W. H. Zhang, A.W. Xu, One-step *in situ* growth of iron-nickel sulfide nanosheets on FeNi alloy foils: high-performance and self-supported electrodes for water oxidation, *Small* 13 (2017) 1604161, <https://doi.org/10.1002/smll.201604161>.

[40] M.J. Wang, X.Q. Zheng, L.L. Song, X. Feng, Q. Liao, J. Li, L. Li, Z.D. Wei,  $Fe_3O_4/FeS_2$  heterostructures enable efficient oxygen evolution reaction, *J. Mater. Chem. A* 8 (2020) 14145–14151, <https://doi.org/10.1039/c9ta13775k>.

[41] Y.M. Bi, Z. Cai, D.J. Zhou, Y. Tian, Q. Zhang, Q. Zhang, Y. Kuang, Y.P. Li, X.M. Sun, X. Duan, Understanding the incorporating effect of  $Co^{2+}/Co^{3+}$  in NiFe-layered double hydroxide for electrocatalytic oxygen evolution reaction, *J. Catal.* 358 (2018) 100–107, <https://doi.org/10.1016/j.jcat.2017.11.028>.

[42] K.H. Wang, K.L. Sun, T.P. Yu, X. Liu, G.X. Wang, L.H. Jiang, G.W. Xie, Facile synthesis of nanoporous Ni-Fe-P bifunctional catalysts with high performance for overall water splitting, *J. Mater. Chem. A* 7 (2019) 2518–2523, <https://doi.org/10.1039/c8ta10856k>.

[43] G.Q. Zhao, J. Zou, L.K. Liu, J. Hu, J.A. Yu, F.P. Jiao, Photocatalytic fixation of nitrogen to ammonia by NiFe-LDH-derived sulfide microspheres, *J. Mater. Sci. - Mater. Electron.* 32 (2021) 13396–13408, <https://doi.org/10.1007/s10854-021-05918-2>.

[44] Y. Tan, X. Xu, Q. Li, X.H. Chen, Q.J. Che, Y.S. Chen, Y.W. Long, Constructing ultrathin  $FeS/FeO_2H@Fe$  nano-sheets for highly efficient oxygen evolution reaction, *J. Colloid Interface Sci.* 594 (2021) 575–583, <https://doi.org/10.1016/j.jcis.2021.03.085>.

[45] K.L. Guo, Y.T. Wang, S.Z. Yang, J.F. Huang, Z.H. Zou, H.R. Pan, P.S. Shinde, S. L. Pan, J.E. Huang, C.L. Xu, Bonding interface boosts the intrinsic activity and durability of  $NiSe@Fe_2O_3$  heterogeneous electrocatalyst for water oxidation, *Sci. Bull.* 66 (2021) 52–61, <https://doi.org/10.1016/j.scib.2020.06.003>.

[46] L.Y. Hu, R.S. Xiao, X. Wang, X.S. Wang, C.L. Wang, J. Wen, W.L. Gu, C.Z. Zhu, MXene-induced electronic optimization of metal-organic framework-derived CoFe LDH nanosheet arrays for efficient oxygen evolution, *Appl. Catal. B-Environ.* 298 (2021), 120599, <https://doi.org/10.1016/j.apcatb.2021.120599>.

[47] L. Yan, Z.Y. Xu, X.A. Liu, S. Mahmood, J.L. Shen, J.Q. Ning, S. Li, Y.J. Zhong, Y. Hu, Integrating trifunctional Co@NC-CNTs@NiFe-LDH electrocatalysts with arrays of porous triangle carbon plates for high-power-density rechargeable Zn-air batteries and self-powered water splitting, *Chem. Eng. J.* 446 (2022), 137049, <https://doi.org/10.1016/j.cej.2022.137049>.

[48] L. Dai, Z.N. Chen, L.X. Li, P.Q. Yin, Z.Q. Liu, H. Zhang, Ultrathin Ni(0)-embedded  $Ni(OH)_2$  heterostructured nanosheets with enhanced electrochemical overall water splitting, *Adv. Mater.* 32 (2020) 1906915, <https://doi.org/10.1002/adma.201906915>.

[49] P.V. Shinde, P. Mane, B. Chakraborty, C.S. Rout, Spinel  $NiFe_2O_4$  nanoparticles decorated 2D  $Ti_2C_2$  MXene sheets for efficient water splitting: experiments and theories, *J. Colloid Interface Sci.* 602 (2021) 232–241, <https://doi.org/10.1016/j.jcis.2021.06.007>.

[50] J.X. Chen, Q.W. Long, K. Xiao, T. Ouyang, N. Li, S.Y. Ye, Z.Q. Liu, Vertically-interlayered  $NiFeP/MXene$  electrocatalyst with tunable electronic structure for high-efficiency oxygen evolution reaction, *Sci. Bull.* 66 (2021) 1063–1072, <https://doi.org/10.1016/j.scib.2021.02.033>.

[51] Q.J. Che, Q. Li, X.H. Chen, Y. Tan, X. Xu, Assembling amorphous (Fe-Ni)Co-x-OH/ $Ni_3S_2$  nanohybrids with S-vacancy and interfacial effects as an ultra-highly efficient electrocatalyst: inner investigation of mechanism for alkaline water-to-hydrogen/oxygen conversion, *Appl. Catal. B-Environ.* 263 (2020), 118338, <https://doi.org/10.1016/j.apcatb.2019.118338>.

[52] M.R. Zhang, T.T. Wang, H.Y. Cao, S.S. Cui, P.W. Du, Self-supported  $Ni_2P$  nanosheets on low-cost three-dimensional Fe foam as a novel electrocatalyst for efficient water oxidation, *J. Energy Chem.* 42 (2020) 71–76, <https://doi.org/10.1016/j.jec.2019.06.010>.